Theoretical Description of Dynamic Transmission Characteristics in MDM Waveguide Aperture-Side-Coupled with Ring Cavity

Yan Deng[1] · Guangtao Cao[1] · Yunwen Wu[1] ·
Xiaoqing Zhou[1] · Wenhu Liao[1]

Abstract We investigate the dynamic transmission characteristics in metal-dielectric-metal (MDM) waveguide aperture-side-coupled with ring cavity. Assuming the aperture as a resonator, a theoretical model was established to describe the formation and evolution mechanisms of the spectral responses in circular ring structure, and the theoretical results are in good agreement with the finite-difference time-domain (FDTD) simulations. In particular, combining Maxwell's equations and field distributions, the analytical theory is also applicable to other aperture-side-coupled ring nanostructures, which highlights the utility of the theoretical description. The results may pave the way towards controlling light in highly integrated optical circuits.

Introduction

Surface plasmon polaritons (SPPs) propagating along the metal-dielectric interface hold potential applications in highly integrated optical circuits due to their ability of breaking the diffraction limit and manipulating light in the nanoscale domain [1, 2]. To date, different types of nanoplasmonic waveguiding configurations have been proposed, including metallic nanowires [3, 4], metallic nanoparticle arrays [5], and V grooves in metal substrates [6]. Among various plasmonic guiding structures, MDM waveguides have attracted tremendous research interest because of strong localization with acceptable propagation length, zero bend losses, and ease of fabrication [7, 8].

Owning to the unique feature of MDM waveguide, numerous optical devices have been theoretically predicted and experimentally demonstrated in recent years [9–13], such as splitter [14, 15], bend [16, 17], Y-shaped combiner [18], coupler [19, 20], Mach–Zehnder interferometer [21], and buffer [10–12, 22, 23]. Moreover, a variety of wavelength-select structures based on MDM waveguide have been demonstrated, including tooth-shaped filter [24–26], multichannel filter [27], band-pass filter with disk resonator [28], band-stop filter with rectangular ring resonator [29–31], and channel drop filter with circular ring resonator [32]. For previous studies, 2D MDM-based resonant structures can be mainly categorized as ring [29–32], stub [24–26], and cavity [28, 33]. Nanoplasmonic ring resonator is commonly used as resonant structure to achieve the functions of optical communications, signal processing, and optically preamplified receiver [34]. Due to the tight mode confinement in MDM waveguide, even with state-of-art electron beam or ion beam lithography, resonator excitation via evanescent coupling is both inefficient and challenging to realize. Therefore, diffraction by small apertures was proposed to realize effective coupling [35–37], and an analytical theory is highly desirable for the manipulation of SPPs in MDM waveguide aperture-side-coupled with ring cavity.

In this paper, to investigate the spectral responses in plasmonic system composed of MDM waveguide aperture-side-coupled to circular ring cavity, we assume the aperture as a resonator and derive an analytical expression based on the temporal coupled mode theory (CMT) [38]. To validate the

✉ Guangtao Cao
  caoguangtao456@126.com

[1] College of Physics, Mechanical and Electrical Engineering, Jishou University, Jishou 416000, China

feasibility of the theoretical model, we have compared it with the FDTD method. Interestingly, combining Maxwell's equations and field distributions, the theoretical description is also applicable to other aperture-side-coupled ring cavity structures, such as square ring, elliptical ring, polygonal ring, and so on. Therefore, this work may have potential applications for constructing the high-density plasmonic circuits.

Analytical Model

Figure 1a schematically depicts MDM bus waveguide aperture-side-coupled to a circular ring cavity. The insulator and metal in the structure are air and silver, respectively. The frequency-dependent relative permittivity of silver is characterized by Drude model $\varepsilon(\omega)=1-\omega_p^2/(\omega^2+i\omega\gamma_p)$, with $\omega_p=1.38\times10^{16}$ rad/s and $\gamma_p=2.73\times10^{13}$ rad/s. These parameters fit the experimental results [39] quite well in the visible and near-infrared spectral range. ω is the angular frequency of incident light. The main structure parameters are the width of bus waveguide, circular ring cavity and aperture (w), radius of the circular ring cavity (R), and gap between the bus waveguide and circular ring cavity (g).

Here, the equivalent theoretical model is used to account for the dynamic transmission characteristics of the proposed structure, as illustrated in Fig. 1b. Assuming the aperture center as a reference plane, the aperture is taken as a resonator. S_{+hn} and S_{-hn} (h, $n=1, 2$) stand for the incoming and outgoing waves into the resonator, respectively. The temporal evolution of energy amplitude for the resonator can be written as

$$\frac{da}{dt} = \left(j\omega_0-\frac{\omega_0}{Q_i}-\frac{\omega_0}{2Q_1}-\frac{\omega_0}{2Q_2}\right)a + S_{+21}e^{j\theta_0}\sqrt{\frac{\omega_0}{2Q_2}} + S_{+11}e^{j\theta_1}\sqrt{\frac{\omega_0}{2Q_1}}$$
$$+ S_{+12}e^{j\theta_2}\sqrt{\frac{\omega_0}{2Q_1}} + S_{+22}e^{j\theta_3}\sqrt{\frac{\omega_0}{2Q_2}}, \tag{1}$$

where Q_i, Q_1, and Q_2 represent cavity quality factors and are related to intrinsic loss, circular ring cavity coupling loss, and waveguide coupling loss, respectively. ω_0 is resonant frequency of the resonator. θ_0 and θ_3 (θ_1 and θ_2) are the phases of coupling coefficients between resonator and bus waveguide (circular ring cavity).

From the conservation of energy, we have

$$S_{-22} = S_{+21}-e^{-j\theta_0}\sqrt{\frac{\omega_0}{2Q_2}}a, \tag{2}$$

$$S_{-11} = S_{+12}-e^{-j\theta_1}\sqrt{\frac{\omega_0}{2Q_1}}a, \tag{3}$$

$$S_{-12} = S_{+11}-e^{-j\theta_2}\sqrt{\frac{\omega_0}{2Q_1}}a, \tag{4}$$

$$S_{+11} = S_{-12}\sigma_1 e^{-j\varphi_1}, \tag{5}$$

$$S_{+12} = S_{-11}\sigma_2 e^{-j\varphi_2}, \tag{6}$$

where σ_1 and σ_2 ($0<\sigma_1<1$ and $0<\sigma_2<1$) are the loss coefficients of SPPs mode per round trip in ring cavity and $\varphi_1=\varphi_2=2\pi R\omega\text{Re}(n_{eff})/c=\varphi$ is the phase shift of SPPs mode in ring cavity. $\text{Re}(n_{eff})$ is the real part of effective index for SPPs in ring cavity [13, 25, 37, 40]. Using the boundary conditions of $S_{+22}=0$, the transmission coefficient through the system can be given by

$$t = \frac{S_{-22}}{S_{+21}} = \frac{j\left(\frac{\omega}{\omega_0}-1\right) + \frac{1}{Q_i} + \frac{1}{2Q_1} - \frac{1}{2Q_1}\left[\dfrac{e^{j(\theta_1-\theta_2)}}{1-\dfrac{e^{j\varphi}}{\sigma_1}} + \dfrac{e^{j(\theta_2-\theta_1)}}{1-\dfrac{e^{j\varphi}}{\sigma_2}}\right]}{j\left(\frac{\omega}{\omega_0}-1\right) + \frac{1}{Q_i} + \frac{1}{2Q_1} + \frac{1}{2Q_2} - \frac{1}{2Q_1}\left[\dfrac{e^{j(\theta_1-\theta_2)}}{1-\dfrac{e^{j\varphi}}{\sigma_1}} + \dfrac{e^{j(\theta_2-\theta_1)}}{1-\dfrac{e^{j\varphi}}{\sigma_2}}\right]}. \tag{7}$$

Fig. 1 **a** Schematic of the plasmonic structure based on a circular ring cavity. **b** Equivalent theoretical model for Fig. 1a
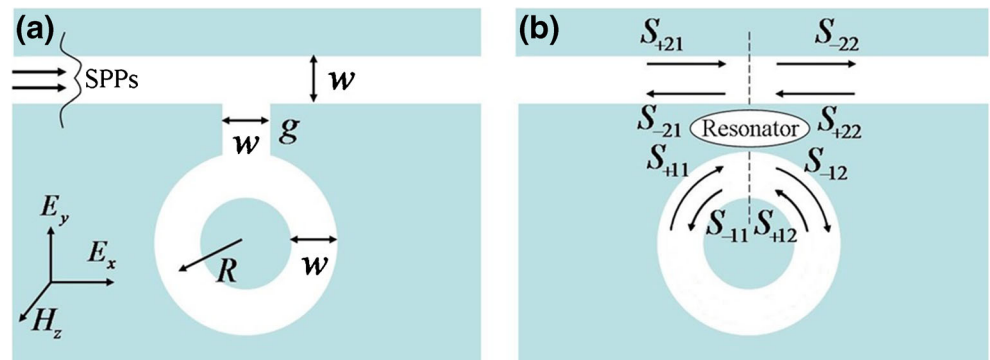
Assuming $\theta_1=\theta_2$ and $\sigma_1=\sigma_2=\sigma$, the theory can be further simplified, so that Eq. 7 reduces to

$$t = \frac{S_{-22}}{S_{+21}} = \frac{j\left(\frac{\omega}{\omega_0}-1\right)+\frac{1}{Q_i}+\frac{1}{2Q_1}-\frac{\sigma}{(\sigma-e^{j\varphi})Q_1}}{j\left(\frac{\omega}{\omega_0}-1\right)+\frac{1}{Q_i}+\frac{1}{2Q_1}+\frac{1}{2Q_2}-\frac{\sigma}{(\sigma-e^{j\varphi})Q_1}}. \quad (8)$$

The transmittance efficiency can be derived as $T=|t|^2$. According to the theoretical analysis mentioned above, we can analyze the spectral responses in MDM waveguide aperture-side-coupled to circular ring cavity.
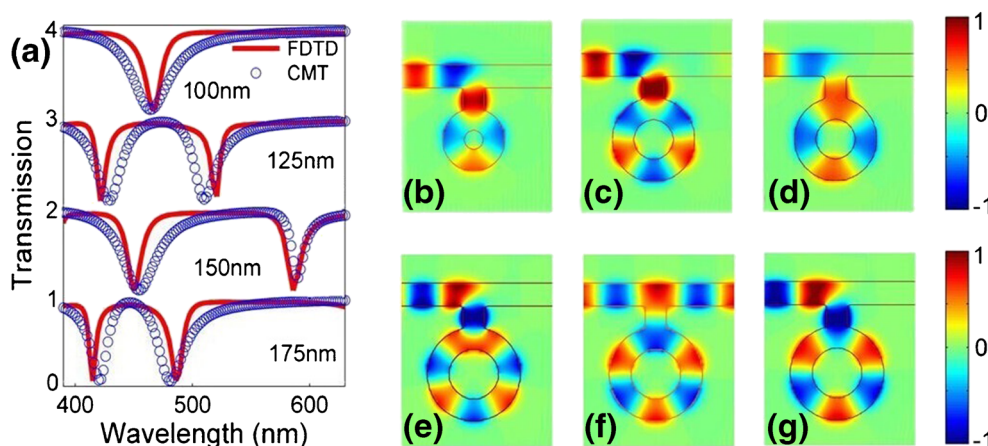
Results and Discussions

Figure 2a shows the transmission spectra with the same constructive parameters ($w=100$ nm, $g=120$ nm), yet with different radius $R=100$, 125, 150, and 175 nm. The circles and solid lines are calculated by the CMT and the FDTD method, respectively. For the theoretical transmission spectra, $\omega_0=4.159\times10^{15}$ rad/s, $Q_i=300$, $Q_1=Q_2=10$, $\sigma=0.96$, and $\text{Re}(n_{eff})=1.26$. It is obvious that the theoretical results agree well with the FDTD simulations, which validates the correctness of the analytical model. So, the theoretical analysis allows us to understand the spectral responses of the plasmonic resonance system explicitly. To get more insight into the physics of the transmission phenomena, in Fig. 2b–g, we plot the magnetic field H_z distributions of the structure at different wavelengths. For the circular ring system in Fig. 1a, the resonance modes are denoted by TM_m (m is the number of node of standing waves in ring cavity). Using the definition of resonance mode, we aim to investigate the evolution of resonant wavelength versus R. Figure 2b corresponds to the resonant wavelength $\lambda=468.7$ nm (TM_4 mode) for the case of $R=100$ nm. Figure 2c, d depicts the z-component magnetic field distributions of transmission dips, for $R=150$, at $\lambda=450.2$ and 585.9 nm corresponding to TM_6 and TM_4 modes, respectively. In Fig. 2e–g, we illustrate the z-component magnetic field patterns at $\lambda=415$ nm (TM_8 mode), 450 and 485.9 nm (TM_6 mode) for $R=175$ nm. The results in Fig. 2b–g are in conformity with the transmission spectra in Fig. 2a.

According to Fig. 2a, we get the wavelength of resonant modes versus R in Fig. 3a. It is seen that, to the radius R of circular ring cavity, TM_4 mode is more sensitive than the TM_6 and TM_8 modes. Moreover, the mode spacing between TM_6 and TM_8 modes keeps unchanged, but the mode spacing between TM_4 and TM_6 modes increases with the increment of R. The small discrepancy between the simulation and analytical results is attributed to the dispersions of effective index n_{eff} and cavity quality factors (Q_i, Q_1, and Q_2).

To exhibit the formation and evolution mechanisms of the spectral responses more explicitly, in Fig. 3b, we plot the transmission spectra versus R and λ by the CMT. Combining Figs. 2a and 3b, one can conclude that the increase of effective waveguide length in ring cavity leads to red shift of resonance modes in the plasmonic structure. If we manipulate the other geometrical or constitutive parameters of the plasmonic system, such as the width or length of the aperture, the width of the ring cavity, and the filling dielectric in the aperture or ring cavity, the analytical model is also consistent with the FDTD method (not shown here). Consequently, the theoretical analysis allows us to understand and predict spectral responses of the plasmonic system as a function of their microscopic

Fig. 2 a Transmission spectra versus different R. The *solid curves* are the simulation results and the *circles* are analytical fits using the CMT. The other geometrical parameters are $w=100$ nm and $g=120$ nm. Field distributions (H_z) of SPPs in the plasmonic structure for $R=100$ nm at wavelength b $\lambda=468.7$ nm. For $R=150$ nm, field distributions (H_z) of SPPs at different wavelengths c $\lambda=450.2$ and d $\lambda=585.9$ nm. For $R=175$ nm, field distributions (H_z) of SPPs at different wavelengths e $\lambda=415$, f $\lambda=450$ and g $\lambda=485.9$ nm
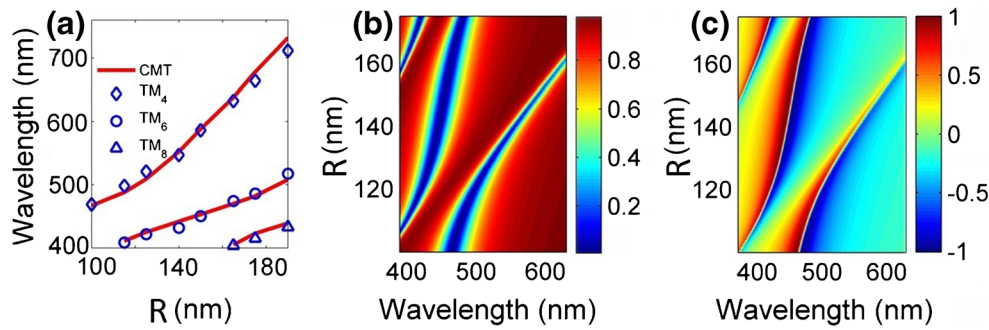
Fig. 3 **a** The resonant wavelengths of the circular ring cavity system versus R, including both the numerical (*dots*) and theoretical (*red solid line*) results. Evolution of **b** transmission spectra and **c** transmission phase shift, obtained by the analytical model, versus R and λ. The other geometrical parameters are $w=100$ nm and $g=120$ nm

parameters, which may indeed be of considerable importance for the design of micro-nano photonic devices.

Slow light in plasmonic structure induces enhanced light–matter interaction, which is one of the most important applications in atom systems. $\tau_g=d\theta/d\omega$ and $\theta=arg(t)$ stand for the optical delay time and transmission phase shift, respectively. Figure 3c shows the transmission phase shift versus R and λ, in which there is a sudden phase jump and the phase slope is negative with respect to λ around the transmission dip. That is to say, the plasmonic system also supports slow group velocities [13, 22, 37], which may be promising for the development of ultra-compact optical buffers. Moreover, the analytical model has been proposed to describe the dynamic transmission characteristics in MDM waveguide aperture-side-coupled with slot cavity [41], whether it is also suitable for other aperture-side-coupled ring cavity structures.

Figure 4a illustrates the schematic of MDM waveguide aperture-side-coupled to square ring cavity. The structural parameters consist of the width of bus waveguide, square ring cavity and aperture (w_s), side lengths of square ring cavity ($L_x=L_y$), and gap between the bus waveguide and square ring cavity (g_s). The perimeter of the square ring is defined as the average of the inner and outer perimeters $L=2(L_x+L_y)$. For the square ring cavity structure, in Fig. 4b, we plot a series of transmission spectra as a function of side length (red solid line). In order to exclude the effects of perimeter of square ring cavity, we also show the transmission spectra for the circular ring cavity system (blue solid line) under the condition that $2\pi R=2(L_x+L_y)=L$. The resonant wavelengths of all modes, as R varies from 175 to 250 nm, are plotted in Fig. 4c. For the square ring system in Fig. 4a, the resonance modes are classified by TM_{ms}. m is also the number of node of standing waves in square ring cavity, and s represents square ring. The resonant modes for circular ring and square ring structures are, respectively, denoted by blue and red solid lines. The corners of square ring structure, as we all know, contribute to the differences in their transmission spectra. It is noted that all the wavelengths of resonance modes increase linearly with increasing perimeter. For the case of $m=4$, the mode spacing

between circular ring cavity and square ring cavity keeps nearly constant with the increase of perimeter, while the mode spacing for other resonant modes ($m=6, 8, 10$) changes.

To investigate the relationship between TM_m and TM_{ms} modes, in Fig. 5a–h, we plot the magnetic field H_z distributions of SPPs at different wavelengths. For the circular ring cavity structure, Fig. 5a–d shows the field distributions of TM_4 ($\lambda=830$ nm), TM_6 ($\lambda=590.2$ nm), TM_8 ($\lambda=474.3$ nm), and TM_{10} ($\lambda=417.2$ nm) modes, respectively, for $R=225$ nm. In Fig. 5e–h, we show the magnetic field profiles of TM_{4s} ($\lambda–751.7$ nm), TM_{6s} ($\lambda=573.2$ nm), TM_{8s} ($\lambda=491.9$ nm), and TM_{10s} ($\lambda=417.2$ nm) modes in the square ring cavity system with $L_x=L_y=353.4$ nm. The perimeter of circular ring cavity is equal to that of the square ring cavity.

For the modes depicted in Fig. 5a–h, the magnetic field standing waves are established in the circular ring and square ring cavities. The outer (inner) perimeter of the square ring is 400 nm longer (shorter) than its perimeter L, but the outer (inner) perimeter of the circular ring resonator is 100π nm longer (shorter) than its perimeter $2\pi R$. According to Maxwell's equations, the antinode (node) of magnetic field locates at the node (antinode) of electric field, and the surface currents and charge densities on ring walls can be, respectively, derived from $n\times H=J$ and $n\cdot D=\sigma$. n is a unit normal vector directed from metal into air. H and D are the magnetic field and electric displacement. From [42], the waveguide length of ring cavity approximately equals to the distance of current flow on the wall. Thus, the effective waveguide length in the circular or square ring cavity can be expressed as

$$L_{eff} = L + \Delta J - \Delta Q, \tag{9}$$

where ΔJ (ΔQ), affected by the structure, denotes the increment (decrement) of waveguide length in the ring cavity.

Due to the uniformity of the circular ring cavity, we get $\Delta J\approx\Delta Q$, which implies that the effective waveguide length in circular ring cavity is approximately equal to its perimeter $2\pi R$. For the square ring cavity, if the node of magnetic field (antinode of electric field) locates at the corner, we get ΔJ

Fig. 4 **a** Schematic of MDM waveguide aperture-side-coupled to square ring cavity. **b** Transmission spectra, obtained by the FDTD method, versus R for circular ring cavity (*blue solid line*) and square ring cavity (*red solid line*), with the condition that $L=2\pi R=2(L_x+L_y)$. The other geometrical parameters are $w=w_s=100$ nm and $g=g_s=120$ nm. **c** The wavelength of the transmission dips in Fig. 4b as a function of R. TM_m and TM_{ms} ($m=4, 6, 8, 10$) denote resonant modes correspond to circular ring and square ring structures, respectively
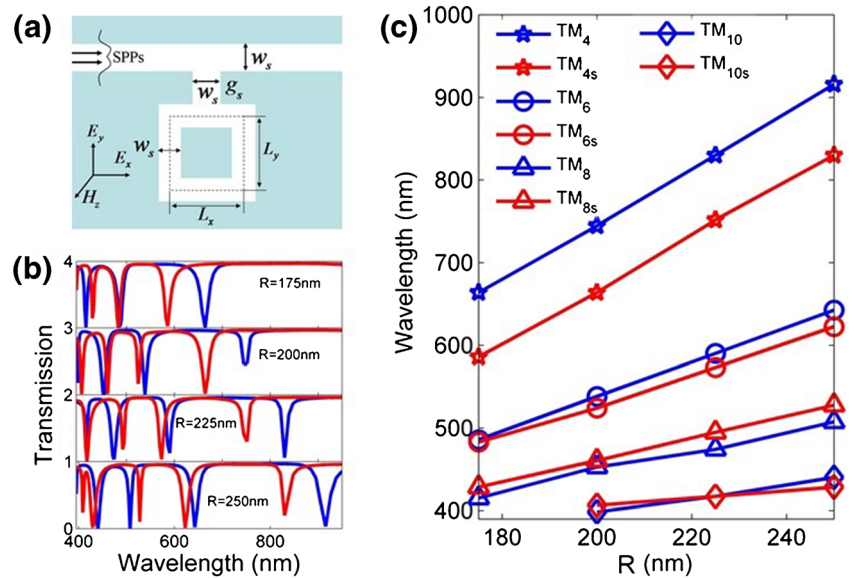
$<\Delta Q$. As shown in Fig. 5e, the magnetic field (electronic field) in square ring cavity has its maximum amplitude at the ring faces (corners), which leads to $\Delta J<\Delta Q$, so the effective waveguide length in square ring cavity is shorter than that in circular ring cavity ($L_{eff}<L=2\pi R$). Based on the analytical theory, the evolution mechanisms of resonant modes in square ring or circular ring can be explained in terms of effective waveguide length. The shorter waveguide length introduces smaller φ, and then the resonant mode shifts to shorter wavelength. Therefore, for the case of $R=225$ nm, the TM_{4s} mode presents blue-shift when compared with TM_4 mode. On the contrary, in Fig. 5g, the magnetic field antinode around the corner leads to $\Delta J>\Delta Q$, which lengthens the effective waveguide length L_{eff} in square ring cavity and contributes to the red shift of TM_{8s} mode relative to TM_8 mode for $R=225$ nm. The relation between TM_6 and TM_{6s} (TM_{10} and TM_{10s} modes) modes is also dependent on the effective waveguide lengths of them. In addition, combining Maxwell's equations and field distributions, we can also qualitatively analyze the effective path L_{eff} in elliptical ring cavity or polygonal ring cavity in this way (not discussed here). Consequently, the theoretical description may provide an in-depth understanding of transmission responses in aperture-side-coupled ring nanostructures.

Fig. 5 Field distributions (H_z) of SPPs for the circular ring cavity structure ($w=100$ nm, $g=120$ nm, $R=225$ nm) at different wavelengths **a** $\lambda=830$, **b** $\lambda=590.2$, **c** $\lambda=474.3$, and **d** $\lambda=417.2$ nm. For the square ring cavity structure ($w_s=100$ nm, $g_s=120$ nm, $L_x=L_y=353.4$ nm), field distributions (H_z) of SPPs at wavelengths **e** $\lambda=751.7$, **f** $\lambda=573.2$, **g** $\lambda=491.9$, and **h** $\lambda=417.2$ nm
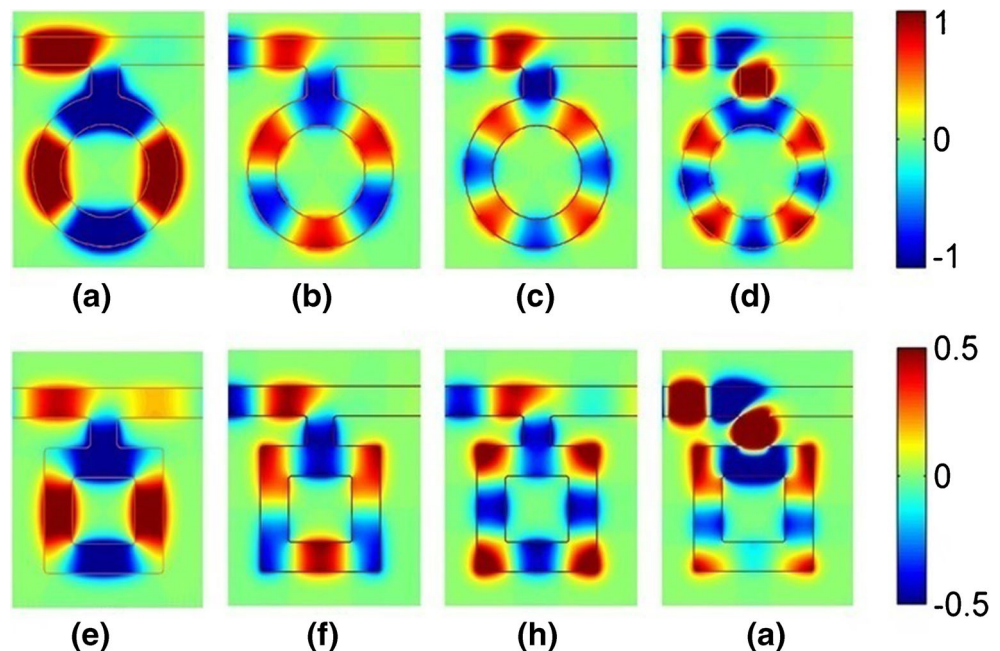
Conclusion

In summary, we have numerically and analytically demonstrated the dynamic transmission characteristics in MDM waveguide aperture-side-coupled with circular ring cavity. The spectral responses obtained theoretically agree well with the rigorous FDTD simulations, which validates the feasibility of the analytical model. Moreover, the theoretical analysis presents the formation and evolution mechanisms of the spectral responses versus microscopic parameters of the circular ring structure. In particular, combining Maxwell's equations and field distributions, we can qualitatively analyze the effective waveguide length L_{eff} in circular ring and square ring cavities, and the analytical theory is also applicable to other aperture-side-coupled ring nanostructures. Therefore, the results may open up avenues for designing sensitive sensor, switches, filters, and slow-light devices in highly integrated optical circuits.

References

1. Barnes WL, Dereux A, Ebbesen TW (2003) Surface plasmon subwavelength optics. Nature 424:824–830
2. Gramotnev DK, Bozhevolnyi SI (2010) Plasmonics beyond the diffraction limit. Nat Photonics 4:83–91
3. Li Q, Qiu M (2013) Plasmonic wave propagation in silver nanowires: guiding modes or not? Opt Express 21:8587–8595
4. Wang W, Yang Q, Fan F, Xu H, Wang ZL (2011) Light propagation in curved silver nanowire plasmonic waveguides. Nano Lett 11:1603–1608
5. Fang ZY, Zhu X (2013) Plasmonics in nanostructures. Adv Mater 25:3840–3856
6. Pile DFP, Gramotnev DK (2005) Plasmonic subwavelength waveguides: next to zero losses at sharp bends. Opt Lett 30:1186–1188
7. Akjouj A, Leveque G, Szunerits S, Pennec Y, Djafari-Rouhani B, Boukherroub R, Dobrzynski L (2013) Nanometal plasmon polaritons. Surf Sci Rep 68:1–67
8. Han ZH, Bozhevolnyi SI (2013) Radiation guiding with surface plasmon polaritons. Rep Prog Phys 76:016402
9. Chen JJ, Li Z, Yue S, Xiao JH, Gong QH (2012) Plasmon-induced transparency in asymmetric T-shape single slit. Nano Lett 12:2494–2498
10. Zhang ZR, Zhang LW, Li HQ, Chen H (2014) Plasmon induced transparency in a surface plasmon polariton waveguide with a comb line slot and rectangle cavity. Appl Phys Lett 104:231114
11. Cai WS, Shin W, Fan SH, Brongersma ML (2010) Elements for plasmonic nanocircuits with three-dimensional slot waveguides. Adv Mater 22:5120–5124
12. Chai Z, Hu XY, Zhu Y, Sun SB, Yang H, Gong QH (2014) Ultracompact chip-integrated electromagnetically induced transparency in a single plasmonic composite nanocavity. Adv Optical Mater 2:320–325
13. Cao GT, Li HJ, Zhan SP, Xu HQ, Liu ZM, He ZH, Wang Y (2013) Formation and evolution mechanisms of plasmon-induced transparency in MDM waveguide with two stub resonators. Opt Express 21:9198–9205
14. Zhang X, Li Z, Chen JJ, Yue S, Gong QH (2013) A dichroic surface-plasmon-polariton splitter based on an asymmetric T-shape nanoslit. Opt Express 21:14548–14554
15. Chheang V, Lee TK, Oh GY, Kim HS, Lee BH, Kim DG, Choi YW (2013) Compact polarizing beam splitter based on a metal-insulator-metal inserted into multimode interference coupler. Opt Express 21:20880–20887
16. Lee TW, Gray S (2005) Subwavelength light bending by metal slit structures. Opt Express 13:9652–9659
17. Guo YN, Wang HN, Reed JM, Pan S, Zou SL (2013) Effective light bending and controlling in a chamber-channel waveguide system. Opt Lett 38:2209–2211
18. Gao H, Shi H, Wang C, Du C, Luo X, Deng Q, Lv Y, Lin X, Yao H (2005) Surface Plasmon polariton propagation and combination in Y-shaped metallic channels. Opt Express 13:10795–10800
19. Rotenberg N, Beggs DM, Sipe JE, Kuipers L (2013) Resonant coupling from a new angle: coherent control through geometry. Opt Express 21:16504–16513
20. Huang Y, Min CJ, Veronis G (2012) Compact slit-based couplers for metal-dielectric-metal plasmonic waveguides. Opt Express 20:22233–22244
21. Bozhevolnyi SI, Volkov VS, Devaux E, Laluet JY, Ebbesen TW (2006) Channel plasmon subwavelength waveguide components including interferometers and ring resonators. Nature 440:508–511
22. Cao GT, Li HJ, Zhan SP, He ZH, Guo ZB, Xu XK, Yang H (2014) Uniform theoretical description of plasmon-induced transparency in plasmonic stub waveguide. Opt Lett 39:216–219
23. Piao XJ, Yu S, Park N (2012) Control of Fano asymmetry in plasmon induced transparency and its application to plasmonic waveguide modulator. Opt Express 20:18994–18999
24. Tao J, Huang XG, Lin X, Zhang Q, Jin X (2009) A narrow-band subwavelength plasmonic waveguide filter with asymmetrical multiple-teeth-shaped structure. Opt Express 17:13989–13994
25. Pannipitiya A, Rukhlenko ID, Premaratne M, Hattori HT, Agrawal GP (2010) Improved transmission model for metal-dielectric-metal plasmonic waveguides with stubs tructure. Opt Express 18:6191–6204
26. Chen JJ, Sun CW, Gong QH (2014) Fano resonances in a single defect nanocavity coupled with a plasmonic waveguide. Opt Lett 39:52–55
27. Luo X, Zou XH, Li XF, Zhou Z, Pan W, Yan LS, Wen KH (2013) High-uniformity multichannel plasmonic filter using linearly lengthened insulators in metal–insulator–metal waveguide. Opt Lett 38:1585–1587
28. Zhan GZ, Liang RS, Liang HT, Luo J, Zhao RT (2014) Asymmetric band-pass plasmonic nanodisk filter with mode inhibition and spectrally splitting capabilities. Opt Express 22:9912–9919
29. Hosseini A, Massoud Y (2007) Nanoscale surface plasmon based resonator using rectangular geometry. Appl Phys Lett 90:181102
30. Zand I, Abrishamian MS, Berini P (2013) Highly tunable nanoscale metal-insulator-metal split ring core ring resonators (SRCRRs). Opt Express 21:79–86
31. Zand I, Mahigir A, Pakizeh T, Abrishamian MS (2012) Selective-mode optical nanofilters based on plasmonic complementary split-ring resonators. Opt Express 20:7516–7525
32. Xiao SS, Liu L, Qiu M (2006) Resonator channel drop filters in a plasmon-polaritons metal. Opt Express 14:2932–2937
33. Hu F, Yi H, Zhou Z (2011) Band-pass plasmonic slot filter with band selection and spectrally splitting capabilities. Opt Express 19:4848–4855
34. Chen CH (2014) Plasmonic bandpass filter with cascaded rectangular ring resonators. Opt Lett 39:3227–3230

35. Han Z, Van V, Herman WN, Ho PT (2009) Aperture-coupled MIM plasmonic ring resonators with sub-diffraction modal volumes. Opt Express 17:12678–12684

36. Nielsen MP, Elezzabi AY (2013) Ultrafast all-optical modulation in a silicon nanoplasmonic resonator. Opt Express 21:20274–20279

37. Lu H, Liu XM, Mao D (2012) Plasmonic analog of electromagnetically induced transparency in multi-nanoresonator-coupled waveguide systems. Phys Rev A 85:053803

38. Haus HA (1984) Waves and fields in optoelectronics. Prentice-Hall, Englewood Cliffs, Chapter 7

39. Palik ED (ed) (1985) Handbook of optical constants of solids. Academic, Boston

40. Dionne JA, Sweatlock LA, Atwater HA, Polman A (2006) Plasmon slot waveguides: towards chip-scale propagation with subwavelength-scale localization. Phys Rev B 73:035407

41. Cao GT, Li HJ, Deng Y, Zhan SP, He ZH, Li BX (2014) Systematic theoretical analysis of selective-mode plasmonic filter based on aperture-side-coupled slot cavity. Plasmonics 9:1163–1169

42. Wang YH, Wang YQ, Zhang Y, Liu ST (2009) Transmission through metallic array slits with perpendicular cuts. Opt Express 17:5014–5022